IEEE Access
Multidisciplinary | Rapid Review | Open Access Journal

Received August 26, 2021, accepted September 11, 2021, date of publication September 14, 2021,
date of current version September 22, 2021.

Digital Object Identifier 10.1109/ACCESS.2021.3112587

EMI Reduction via Resonator Coils in Glassless Integrated Domestic Induction Systems

EMILIO PLUMED[1], (Member, IEEE), IGNACIO LOPE[2,3], (Member, IEEE), AND JESUS ACERO[1], (Senior Member, IEEE)

[1]Department of Electronic Engineering and Communications, University of Zaragoza, 50018 Zaragoza, Spain
[2]Department of Applied Physics, University of Zaragoza, 50009 Zaragoza, Spain
[3]B/S/H/ Home Appliances, 50016 Zaragoza, Spain

Corresponding author: Emilio Plumed (eplumed@unizar.es)

This work was supported in part by the Spanish Ministry of Science and Innovation [Ministerio de Ciencia e Innovación (MICINN)] and Agencia Estatal de Investigación (AEI) under Project PID2019-103939RB-I00, in part by the European Union (EU) through European Regional Development Fund [Fondo Europeo de Desarrollo Regional (FEDER)] Program, in part by BSH Hausgeräte GmbH , and in part by the Gobierno de Aragón-FSE 2014-20 under Grant IIU/2023/2017.

ABSTRACT This paper explores the magnetic flux emissions of induction heating systems compared with inductively coupled heating systems. Inductively coupled heating uses a resonator coil attached to the ferromagnetic load in order to improve energy transfer from the appliance to the load. The magnetic flux emissions of both kinds of systems are simulated, and their dependence on coil current and turn number is outlined. The paper focuses on emitted near field, whose measurement and limits are determined by norm. Several prototypes are developed and tested to verify the simulations.

INDEX TERMS Induction heating, appliances, inductive power transmission, electromagnetic interference.

I. INTRODUCTION

Domestic induction heating (IH) technology has evolved during the last 20 years enabling the development of induction cooktops, which nowadays can be considered standard consumer electronics products [1]. The advantages of these apparatus in contrast with traditional cooking systems (gas, resistive or radiant) are recognized by an increasing number of users worldwide. At the heart of the success of the induction cooktops lies its contactless heat generation capability and the advances and innovations of the enabling technologies. Nowadays, an intense research activity is still detected in this field, mainly focused on improving the performance and reducing the cost of current cooktops. This research activity encompasses power electronics converters for an efficient use of the energy [2], [3], coil arrangements for the improvement of the user flexibility [4]–[6], load identification systems [7], [8], sensing functionalities [9]–[11], inductor PCB implementations [12], magnetic materials [13], robotized mobile inductors [14], or adapting non-metallic cookware for induction cooktops [15].

Induction heating cooktops generates a variable magnetic field by means of a planar inductor. Consequently, each burner of an induction cooktop can be regarded as a wireless power transmitter. This fact is inspiring new applications or features of induction cooktops. Currently, the Wireless Power Consortium is launching a cordless kitchen standard, which is built on the success of the Qi standard [16]. This standard covers the field of cooktops that deliver up to 2200 W to smart cordless kitchen appliances [17]. Moreover, induction technology is also favouring the development of wide and clear worktops, which incorporate the cooking functionality without the need to build the appliance into the worktop, by placing inductors beneath its surface [18], as it is illustrated in Fig. 1. The main improvements of glassless systems versus conventional IH systems are their aesthetics, the increase of multi-function working area and the ease of cleaning.

The under-worktop arrangement faces technological challenges mainly derived from the air gap between the inductor and the cookware, which is higher than in conventional cooktops. This fact reduces the global efficiency of the power transference and increases the leakage magnetic flux [19]. In some cases, the decrease of the efficiency compromises the feasibility of practical applications because a substantial reduction of the rated power should be adopted. Several authors have proposed solutions based on the use of intermediate coils, also known as resonators or relay coils. Formerly these solutions were developed for wireless power transfer (WPT) applications [20]–[24] and subsequently

The associate editor coordinating the review of this manuscript and approving it for publication was Wenjie Feng.

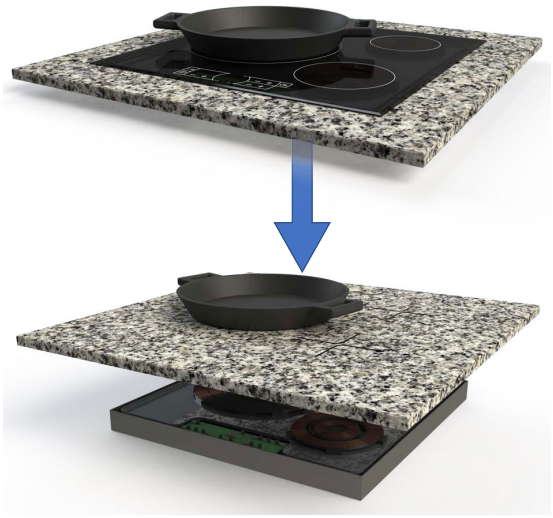

FIGURE 1. Illustration of the induction heating evolution: from traditional cooktops to wireless-power-transfer worktop surfaces.

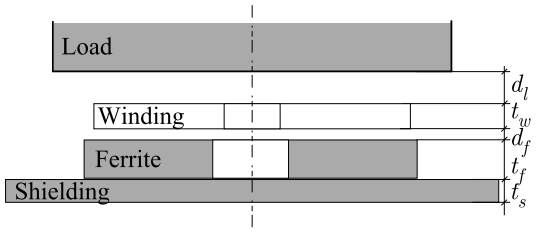

FIGURE 2. Basic induction heating system comprising the planar windings, ferrites, aluminum shielding and vessel.

they have been applied to domestic induction systems [5], [25]–[27], which is referred as inductively coupled heating (ICH) in this paper. The effectiveness of these arrangements is patent, especially regarding the efficiency and heating performance.

Most reservations of induction cookers prospective users concern the electromagnetic emissions [28]. Nevertheless, IH appliances must be compliant with the electromagnetic compatibility (EMC) existing regulations for commercial apparatus. Regulations pursue the reduction of both the electromagnetic levels in the users and the magnetic interference levels in other surrounding electrical devices. The electromagnetic emissions of induction cookers are concerned by two documents. First, the International Commission on Non-Ionizing Radiation Protection [29] proposed recommendations about user exposure to time-varying electromagnetic fields. Second, measurement methods for electromagnetic fields of household appliances with regard to human exposure were regulated by the International Electrotechnical Commission, IEC [30], later adapted by the local regulatory committees [31]. In the past, electromagnetic-compatibility-oriented analysis of conventional induction arrangements were conducted in order to predict emission levels [32] and to propose compliance-focused solutions [33], which were based on spread spectrum technique [34].

Several works report that emission level of commercial cooktops are below the existing regulations. [35]–[37]. However, the compliance of the above mentioned large-air-gap arrangements with the EMC regulations is still pending of an appropriate analysis and experimental verification. This paper aims to analyze the electromagnetic emissions of domestic emerging IH applications where the load is placed at higher distance than in conventional cooktops. The study includes both single-coil and coil-and-resonator arrangements. Both kinds of system are compared throughout the paper. The paper is organized as follows. Section II establishes the measurement method and limits of near emitted magnetic field. Section III introduces the finite element simulation of single inductor IH systems and presents some magnetic flux results. Section IV expands the simulation to ICH systems of analogous geometry. Section V presents the experimental results, comparing both kind of systems. Finally, section VI presents the conclusions drawn from this work.

II. MEASURING PROCEDURES AND METHODS FOR MAGNETIC FIELDS

Proper estimation of field emissions should be in accordance with the standards. Near field emission measurement procedures and methods for magnetic fields are specified in the IEC 62233:2005 standard [30]. This standard sets that the magnetic field should be measured at a horizontal distance from the appliance to the probe, d_{probe}, of 30 cm from each side of the device along a vertical line, and it should be averaged over an area of 100 cm^2 in order to avoid inhomogeneities. The test vessel must have the same diameter of the inductor, or slightly bigger. Moreover, the limit recommended by the 1998 ICNIRP guidelines is 6.25 µT rms for the range comprised from 800 Hz to 150 kHz for the general public [29]. The frequencies used in IH cookers fall in this range. Newer ICNIRP recommendations [38] have increased the general public exposure limit in the range between 3 kHz and 10 MHz to 27 µT, but they have yet to be included in newer home appliance standards and regulations.

According to this standard, near field commercial probes consist of three perpendicular and circular loops of area $S_{\text{loop}} = 100\,\text{cm}^2$. Considering that the loop surfaces are aligned with the three directions of an arbitrary orthonormal coordinate system $(\hat{e}_1, \hat{e}_2, \hat{e}_3)$:

$$\mathbf{B} = B_{e_1}\hat{e}_1 + B_{e_2}\hat{e}_2 + B_{e_3}\hat{e}_3, \tag{1}$$

each loop provides the average of the magnetic flux density according to this expression:

$$B_{e_i,\text{av}} = \frac{1}{S_{\text{loop}}}\int_{S_{e_i}} B_{e_i}\, dS_{e_i}, \quad i = 1, 2, 3, \tag{2}$$

where the coordinate basis is usually cartesian in simulation. The magnitude specified in the IEC 62233:2005 standard is

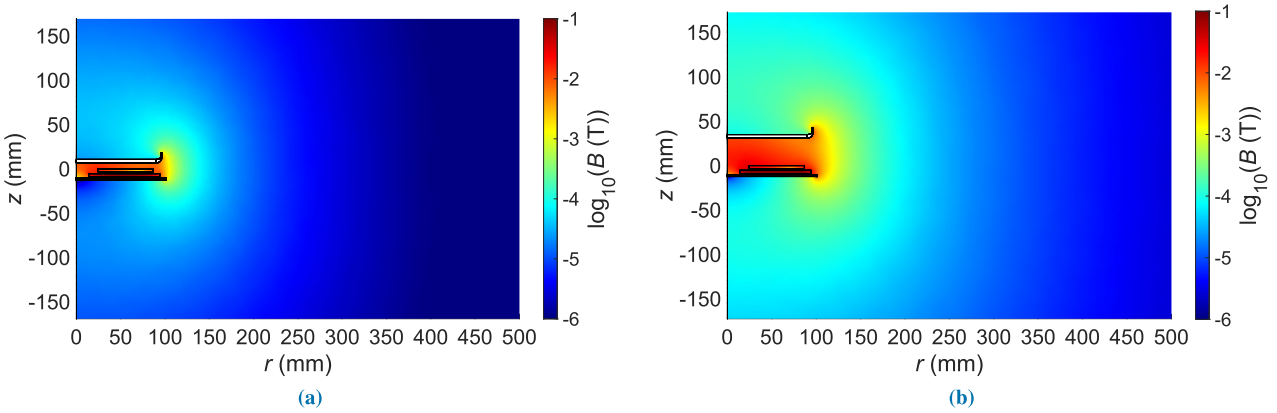

FIGURE 3. Decimal logarithm of magnetic flux produced to deliver 3000 W to the load at 30 kHz and d_l of (a) 6 mm, (b) 30 mm.

the root mean square norm of the magnetic flux density, i.e:

$$B_{\text{norm}} = \text{rms}\left(\sqrt{\left|B_{e_1,\text{av}}\right|^2 + \left|B_{e_2,\text{av}}\right|^2 + \left|B_{e_3,\text{av}}\right|^2}\right). \quad (3)$$

Therefore, any point with a horizontal d_{probe} of 30 cm from the edge of the cooktop, the condition: $B_{\text{norm}}(\mathbf{r}) < 6.25\,\mu\text{T}$, must be met.

Considering (2), (3), the magnetic flux density is required in order to predict the near field emissions of an IH arrangement.

III. MAGNETIC FIELD EMISSIONS OF SINGLE-COIL SYSTEMS

System impedance, and consequently delivered power and emitted field are very dependent on load geometry and material. Load sizes bigger than the inductors produce no change, but smaller diameters do. Horizontal misalignments are detrimental, but can usually be tolerated if they are smaller than half the windings' radius. Systems can be optimized for specific distances, or they can be designed to work adequately for a range of distances, typically between 6 and 30 mm [27].

Fig. 2 shows the arrangement of a single-coil IH system. In this figure, the main vertical distances are shown. The inductor system consists of a n-turn planar windings, the load, a flux concentrator and a shielding plate. In conventional arrangements the distance from the inductor to the load, d_l, is set by the thickness of the cooktop ceramic glass and other insulation elements, which usually ranges from 4 mm to 6 mm. This distance could go up to 50 mm in modern seamless IH arrangements as the one shown in Fig. 1. The diameter of the load is often higher than the diameter of the windings in normal operation. Usually, conventional IH cooktops incorporate an automatic load-size detection system based on the value of the equivalent impedance, which switches off the power when the diameter of the vessel is smaller than the diameter of the windings. The flux concentrator consists of a set of ferrite bars or circular sectors and the shielding is usually an aluminum plate.

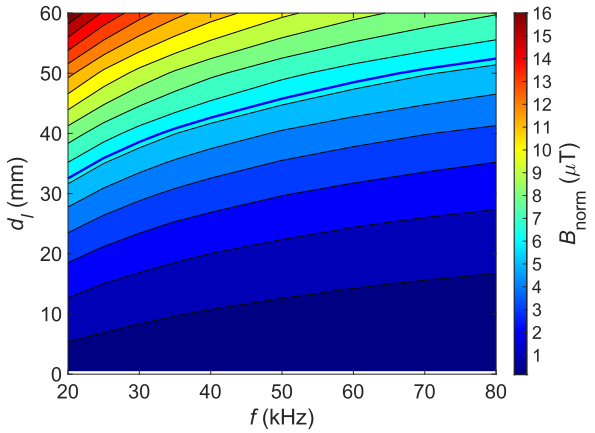

FIGURE 4. Magnetic flux measured by simulated probe when delivering 3000 W to the load for different frequencies and distances. The IEC 62233 [30] limit is highlighted in a thicker blue line.

The field emissions are obtained by means of the COMSOL finite element analysis (FEA) tool. The system of Fig. 2 has axial symmetry and is therefore suitable for 2D simulations. Given that the testing probe requires integration in a 3D field, the 2D solution is revolved and the polar coordinate system is substituted for a cartesian one to use the x, y, z components directly in (3). The following considerations have also been adopted:

- All involved media are considered isotropic and linear. Moreover, dissipative media (aluminum and load) are modelled as an Impedance Boundary Condition (IBC). This model is valid when the skin depth of fields is smaller than the thickness of the media, as occurs in the aluminum and ferromagnetic vessels at the operating frequencies [15].
- Real windings and their cabling structure are modeled by an ideal rectangular cross-sectional constant current density of value $J = n\hat{I}/S_w$, where n is the winding's number of turns, S_w is the cross-sectional area of the winding and $\hat{I}$ is the current amplitude. This assumption

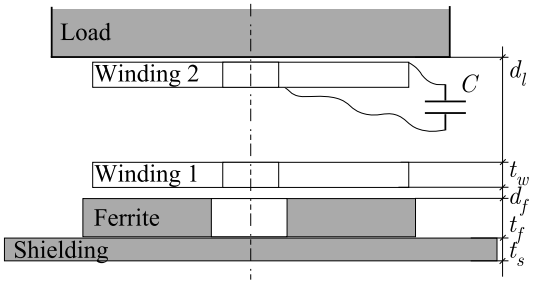

FIGURE 5. Basic structure of an induction heating system with resonator coil.

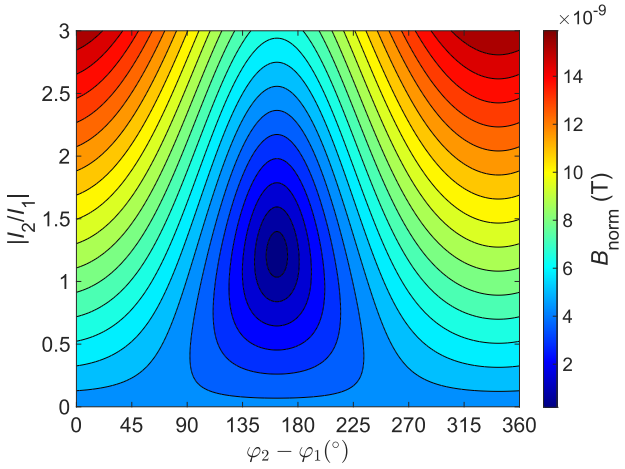

FIGURE 6. Magnetic flux generated by the ICH system with 1 Ampere-turn in the primary inductor at 30 mm and 30 kHz for different current ratios and phase angles.

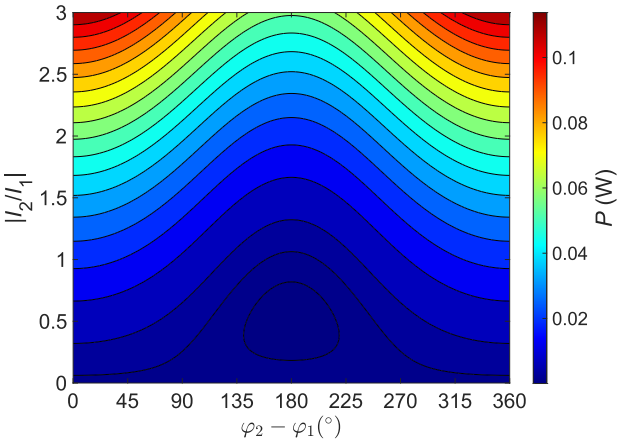

FIGURE 7. Power delivered by the ICH system with 1 Ampere-turn in the primary inductor at 30 mm and 30 kHz for different current ratios and phase angles.

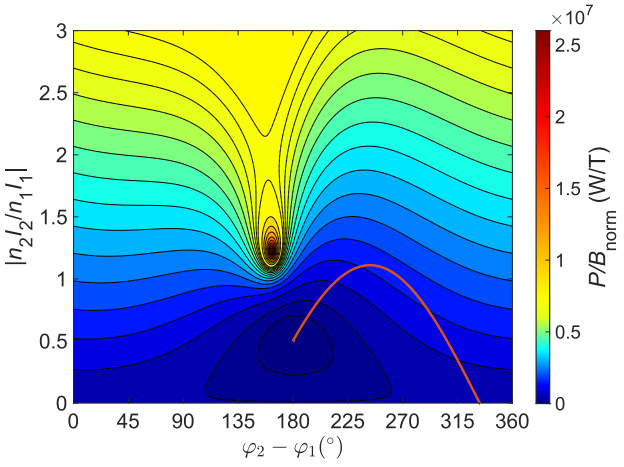

FIGURE 8. Power delivered by the ICH system per emitted magnetic field with 1 Ampere-turn in the primary inductor at 30 mm and 30 kHz for different current ratios and phase angles. The orange line represents the values that can be achieved with the system.

is valid for coils with high density of turns, which is typical in commercial applications.

– Considering that the magnetic field is proportional to number of turns and current amplitude, simulations per turn and per Ampere are carried out, i.e., the input current density is calculated assuming $n = 1$ and $\hat{I} = 1$.

Some simulation results are shown in Fig. 3 for an IH with an inductor of $\phi_{\text{ext}} = 180$ mm external diameter. This figure shows the **B** field for two different distances $d_l = 4$ mm and $d_l = 30$ mm. As it can be observed, the higher the distance is, the higher is the magnitude of the magnetic field in the surrounding area of the cooktop. Generally speaking, the magnetic field is partially shielded by the load and the shielding is less effective with increasing d_l. For the same reason, when the frequency of the excitation increases the level of B_{norm} decreases. The dependency map of B_{norm} with the distance and frequency is shown in Fig. 4, where the limit of the current standard is also represented. Considering that the rated power is usually supplied at frequencies below 40 kHz, for the depicted inductor of $\phi_{ext} = 180$ mm the maximum allowable distance would be less than 40 mm, which is similar to the thickness of regular worktops. Therefore, commercial solutions of under-worktop IH arrangements could compromise the fulfilment of current regulations. Therefore, an alternative solution is explored in the next section.

IV. MAGNETIC FIELD EMISSIONS OF INDUCTION HEATING SYSTEMS WITH RESONATOR COIL

The use of resonator coils is relatively common in WPT systems in order to improve the coupling between primary and secondary coils and to make them tolerant against misalignment or high d_l. As it was above commented, ICH designers take advantage of this idea for adapting conventional-sized inductors to large vessels or for heating non-ferromagnetic materials. The presence of the load, i.e. a dissipative medium in the system, confers specific characteristics to this approach.

The basic structure of a ICH system with resonator coil is shown in Fig. 5, where the resonator is attached to the load. As the windings' impedance is dependent on the properties

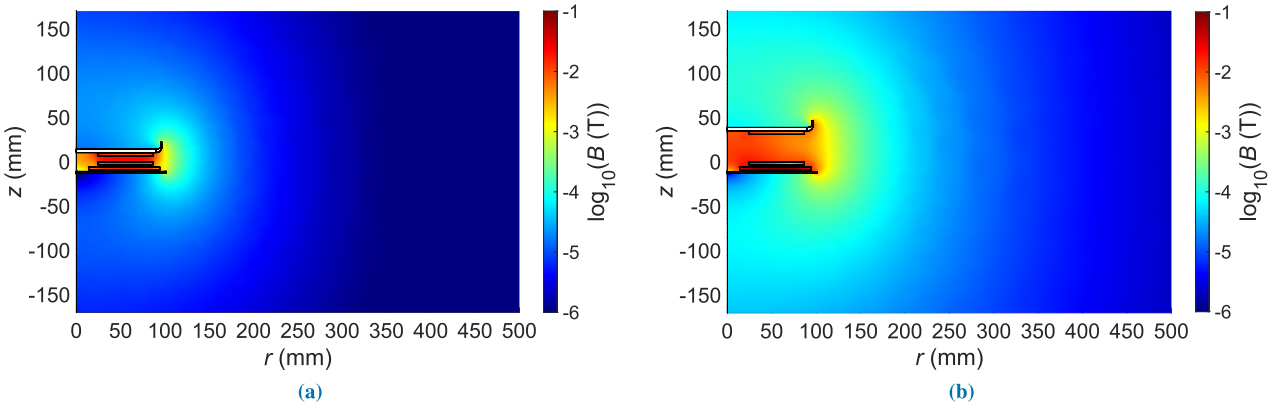

FIGURE 9. Decimal logarithm of magnetic flux produced by the ICH system to deliver 3000 W to the load at 30 kHz and d_l of (a) 6 mm, (b) 30 mm.

of the ferromagnetic material of the load, it is preferable to make the inductor non-detachable. In this structure the first winding wirelessly transfers energy to the second winding, which inductively heats the load. In this figure, the capacitor is designed to shift the phase of the winding current and therefore to achieve a constructive addition of the fields generated by both coils at the bottom of the vessel. Current phase difference between the primary and resonator coils determines the level emission of the magnetic flux density at the positions of the near field probe. Assuming harmonic analysis, the current of each inductor is defined as follows:

$$\begin{cases} I_1 = \hat{I}_1 \cdot e^{(j\omega t+\varphi_1)} \\ I_2 = \hat{I}_2 \cdot e^{(j\omega t+\varphi_2)} \end{cases} \tag{4}$$

where $\hat{I}_1$, $\hat{I}_2$ are the current amplitude of each inductor, ω is the angular frequency and φ_1, φ_2 are the phase of the inductor currents. Therefore, the phase difference between the inductor currents is $\varphi = \varphi_1 - \varphi_2$. Moreover, the field generated by each inductor can be obtained by means of:

$$\mathbf{H}_i(\mathbf{r}, \varphi_i) = n_i \cdot \mathbf{H}_{i,\mathrm{pt,pA}}(\mathbf{r}) \cdot \hat{I}_i(\varphi_i) \quad i = 1, 2 \tag{5}$$

where subscripts pt, pA denote per turn and per Ampere magnitudes, respectively, and $\mathbf{r}$ is the position vector of the point where the field is calculated. Consequently, the total field at an arbitrary position is:

$$\mathbf{H}(\mathbf{r}, \varphi) = \mathbf{H}_1(\mathbf{r}, \varphi_1) + \mathbf{H}_2(\mathbf{r}, \varphi_2), \tag{6}$$

and considering that the near field probe is placed in the air:

$$\mathbf{B}(\mathbf{r}, \varphi) = \mu_0 \mathbf{H}(\mathbf{r}, \varphi). \tag{7}$$

It would be more accurate to say that $\mathbf{B}$ is separately dependent on φ_1 and φ_2, but the standard measurement only needs its rms norm, as shown in (3).

The simulated geometry in this case is very similar to the one in the previous section, where the resonator coil is of the same size of the primary inductor and it is placed directly below the load. For a fixed I_1, the magnetic flux generated by the system freely changing $|I_2|$ and φ_2 in simulation is shown in Fig. 6. When the currents are in phase, the fields have a constructive effect that increases the total radiated field when I_2 increases, as could be expected. When the currents are in near opposite phase, there is a current ratio that minimizes the radiated field.

TABLE 1. Prototype parameters.

System	n_1	n_2	C_1	C_2
IH	32	–	200 nF	–
ICH 400 nF	19	19	480 nF	400 nF
ICH 800 nF	19	19	480 nF	800 nF

Phase and amplitude differences between inductor currents also determine the delivered power on the vessel's bottom surface [39]. Therefore, the effect of the phase on the delivered power is also investigated. The power can be obtained as the flux of the Poynting's vector at the vessel's bottom surface, which in the harmonic regime is defined as follows:

$$\mathbf{S}(\mathbf{r}, \varphi) = \frac{1}{2}\mathbf{E}(\mathbf{r}, \varphi) \times \mathbf{H}^*(\mathbf{r}, \varphi) \tag{8}$$

where the asterisk in the magnetic field represents the complex conjugate and the electrical field is obtained by adding the electrical field generated by each coil, analogous to (6). Considering the per turn and per Ampere analysis, this equation can be expressed as follows:

$$\mathbf{S}(\mathbf{r}, \varphi) = \frac{1}{2}\sum_i \sum_j n_i n_j \cdot \mathbf{E}_{i,\mathrm{pt,pA}}(\mathbf{r}, \varphi) \times \mathbf{H}^*_{j,\mathrm{pt,pA}}(\mathbf{r}, \varphi) \cdot \hat{I}_i \hat{I}_j \tag{9}$$

Fig. 7 shows the delivered power by the ICH system in simulation with 1 Ampere-turn in the primary and variable I_2 and φ_2 with full freedom. It can be seen that an increase in I_2 increases P, and a phase difference between currents reduces power notably.

In order to minimize B_{norm} while maximizing P, the ratio P/B_{norm} is represented in Fig. 8. The Figure shows that

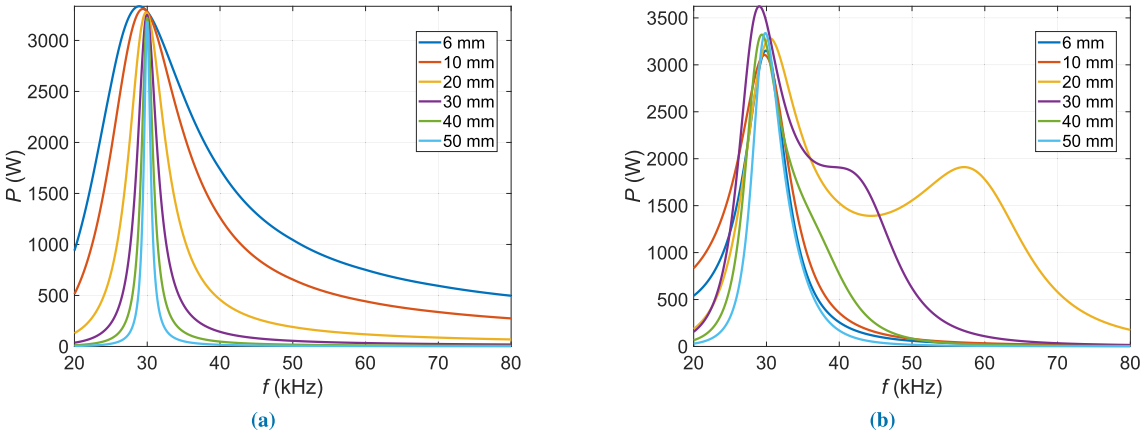

FIGURE 10. Output power for the (a) IH system (b) ICH system.

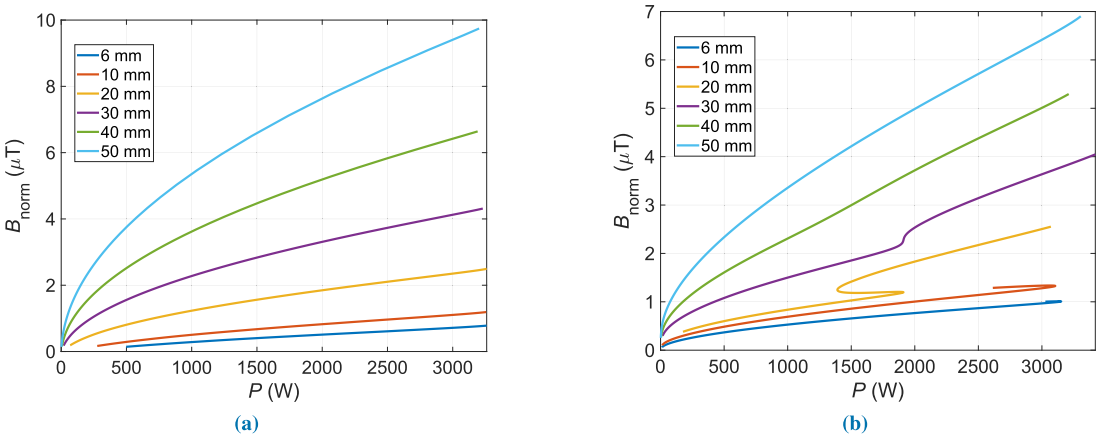

FIGURE 11. Probe calculated magnetic flux for the (a) IH system (b) ICH system.

the optimum operation point is very near the flux minimum observed in Fig. 6, where the power is also smaller, but to a much lesser degree, as seen in Fig. 7. Unfortunately, the current ratio and phase difference cannot be selected freely because only the primary inductor is fed directly, so the only way to change them is via the compensation capacitors. The orange line in Fig. 8 represents the ratios and phase differences that can be reached by design.

Fig. 9 shows the magnetic flux generated by the ICH system at d_l of 6 mm and 30 mm delivering 3000 W at 30 kHz. Comparison with Fig. 3 shows that the ICH system emits less magnetic field for the same frequency and output power.

Ideal designs for the IH and ICH systems have been developed with the objective of reaching 3000 W at 30 kHz for different d_l. Fig. 10 shows P for the IH and ICH system and Fig. 11 shows B_{norm} for both systems calculated at a d_{probe} of 30 cm. The figure shows that for equal frequency and power, the ICH system emits more magnetic flux than the conventional IH system at low d_l. As distance increases, emitted flux increases faster for the IH system than the ICH system, surpassing it when $d_l > 20$ mm.

FIGURE 12. Experimental setup.

Power losses generated in the windings, P_w, and the magnetic shielding, P_{sh}, can be estimated from simulations [40], and the efficiency, η, defined as:

$$\eta = \frac{P_{\text{load}}}{P_{\text{load}} + P_w + P_{\text{sh}}}, \tag{10}$$

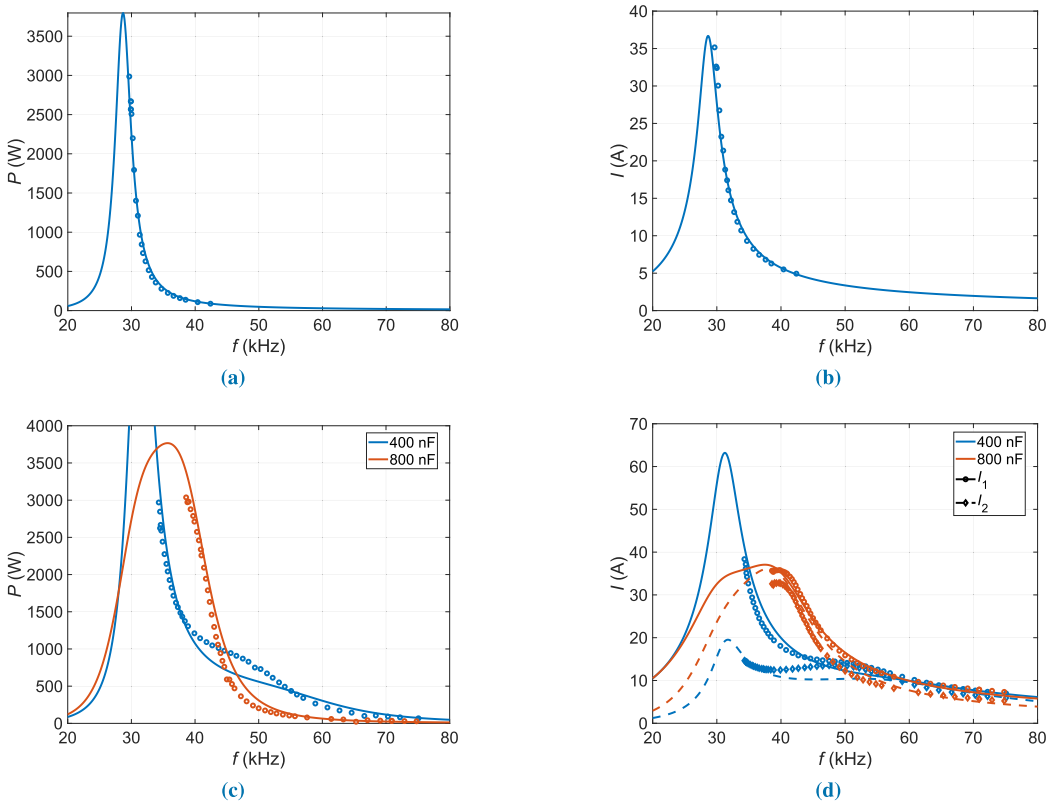

FIGURE 13. Simulated and experimental values of *P* and *I* of the 2D IH and ICH designs. (a) IH *P*, (b) IH *I*, (c) ICH *P*, (d) ICH *I*.

where P_{load} is the power delivered to the load. Although η cannot be measured experimentally, the simulated values for the designs are 92.19 % for the IH system, 96.45 % for the 400 nF ICH system and 96.2 % for the 800 nF ICH system.

V. EXPERIMENTAL RESULTS

In order to reduce the number of required prototypes, the experimental results will focus on the d_l of 30 mm. To achieve similar power and frequency, three 180 mm ∅ windings are prototyped. Two of them have 19 turns, and the third has 32. With these inductors and different compensation capacitor combinations, adequate designs for the IH and ICH systems for 30 mm can be achieved. Table 1 groups the relevant parameters for each prototype. Two very similar ICH prototypes are selected to accentuate the relevance of C_2 selection in terms of emitted magnetic field.

Fig. 12 shows the experimental setup. It maintains the axial symmetry of the 2D simulation with the aluminum shielding disk, the ferrite plane composed of 4 90° circle sectors and a flat ferromagnetic load with the same diameter as the inductors, complying with the norm's size restrictions. The oscilloscope is used to measure voltage and currents in the system. Voltage probes are attached to the inverter output and both inductors, and current probes are attached to the inductors. The field probe is used to take measurements from $d_{\text{probe}} = 0$ cm up to the 30 cm of the IEC 62233:2005 standard [30] in 5 cm increments.

High temperature is not expected to be a problem for the system. The inductors in conventional IH systems can withstand load temperatures, so even though the secondary inductor heats faster, being nearer the load, the steady-state temperature is still manageable. As the capacitors are more sensitive, they have to be placed as far away as possible from the load, preferably with separating thermal insulation material. With these precautions, capacitor temperature can be kept low.

The measured power and currents of each prototype are shown in Fig. 13. The measurements of the IH system match the simulations perfectly. The simulated and experimental values of the 400 nF ICH system are close, with small discrepancies at higher frequencies. The experimental values of the 800 nF ICH system fit the simulated ones very well. The congruent *P* and *I* measurements validate the impedance calculations of the FEA simulations, and they encourage optimism for the magnetic field measurements. Fig. 14 shows the current waveforms for the 800 nF ICH system, where their phase difference can be observed.

Fig. 15 shows the simulated P/B_{norm} ratio for the measured 2D ICH cases with the simulated and measured current ratios and phase differences. While both the 400 nF and 800 nF cases operate along the white line, the point at which the

TABLE 2. Measured and simulated f, P, I, η and B_{norm} values at 3000 W.

System	f (kHz)		P (W)		I_1 (A)		I_2 (A)		η(%)	B_{norm} (μT)		B_{norm} reduction (%)	
	Sim	Exp	Sim	Exp	Sim	Exp	Sim	Exp	Sim	Sim	Exp	$d_{\text{probe}} = 30$ cm	median
IH	29.5	29.6	2967	2986	32.07	35.15	–	–	92.19	3.988	4.257	–	–
ICH 400 nF	34.6	34.3	3030	2969	39.05	38.36	15.03	14.63	96.45	3.665	4.107	3.5	10.3
ICH 800 nF	39.7	39.0	2988	2980	35.66	35.79	34.97	32.78	96.20	3.029	2.398	43.7	45.6

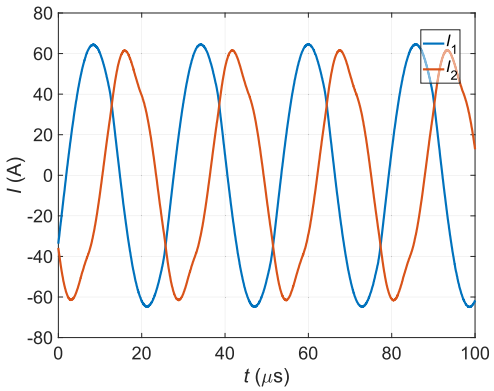

FIGURE 14. Current waveforms in the 800 nF ICH system.

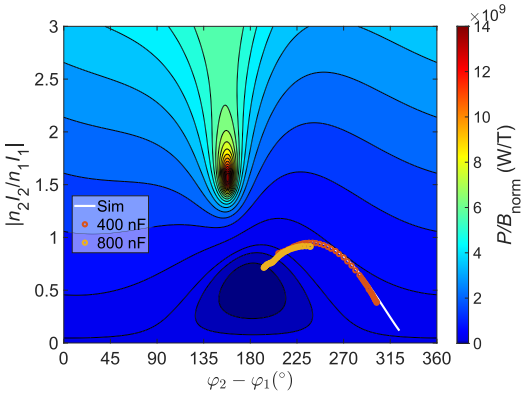

FIGURE 15. Simulated P/B_{norm} ratio for the prototyped 2D ICH cases, with simulated and experimental current ratios and phase differences.

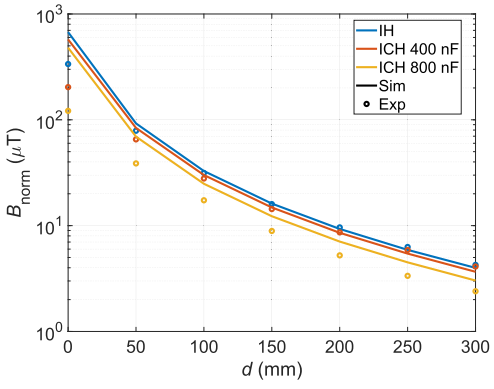

FIGURE 16. Simulated and measured B_{norm} at different d_{probe} for the 2D IH and ICH systems.

system reaches 3000 W, the rightmost one in both cases, is different. From Fig. 15 it can be inferred that the 800 nF design will emit less magnetic field.

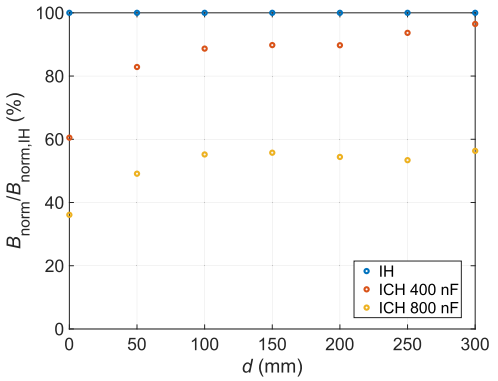

FIGURE 17. Ratio between the measured B_{norm} in all systems with respect to the IH system's.

Fig. 16 shows the measured and simulated B_{norm} for the IH and ICH cases for the d_{probe} range mentioned previously. In all cases, the experimental and simulated values are closest at the farthest d_{probe} and they diverge as they get closer to the system. This is likely due to minor geometry elements in the experimental setup that deviate from the simulated 2D axial symmetry, which are accentuated the closer the probe comes to the systems.

Fig. 17 represents the ratio between the measured B_{norm} of all prototypes with respect to the IH system's. From the IH to the 400 nF ICH system, the emitted field decreases 3.5 % at 30 cm and a median of 10.3 % for all considered d_{probe}. From the IH to the 800 nF ICH system, the field decreases 43.7 % at 30 cm and a median of 45.6 %, more than was expected from the simulations.

For ease of comparison, the simulated and experimental probe values at $d_{\text{probe}} = 30$ cm are shown in Table 2, along with f, P, I and η of all three systems.

VI. CONCLUSION

In this paper it has been proven that ICH systems emit the same amount or less magnetic flux than IH systems of similar geometry and characteristics. Furthermore, a good ICH design focused on EMI can significantly reduce emitted field.

Magnetic field emissions in multiple inductor systems depend on the current ratio and current phase difference, with optimal power to flux points of operation. For ICH in particular, the absolute optimal point cannot be reached, but local optimums can be selected through careful design.

Active elements in the receiver side, such as a DC/DC stage, can add degrees of freedom to reach more favourable

power to magnetic flux emission ratios. Though more costly, those new elements can reduce emissions or increase power for the same magnetic flux.

REFERENCES

[1] J. Acero, J. Burdío, L. Barragán, D. Navarro, R. Alonso, J. García, F. Monterde, P. Hernández, and S. L. I. Garde, "Domestic induction appliances," *IEEE Ind. Appl. Mag.*, vol. 16, no. 2, pp. 39–47, Mar. 2010.

[2] M. Perez-Tarragona, H. Sarnago, O. Lucia, and J. M. Burdio, "Design and experimental analysis of PFC rectifiers for domestic induction heating applications," *IEEE Trans. Power Electron.*, vol. 33, no. 8, pp. 6582–6594, Aug. 2018.

[3] R. C. M. Gomes, M. A. Vitorino, D. A. Acevedo-Bueno, and M. B. D. R. Correa, "Multiphase resonant inverter with coupled coils for AC–AC induction heating application," *IEEE Trans. Ind. Appl.*, vol. 56, no. 1, pp. 551–560, Jan. 2020.

[4] V. T. Kilic, E. Unal, N. Yilmaz, and H. V. Demir, "All-surface induction heating with high efficiency and space invariance enabled by arraying squircle coils in square lattice," *IEEE Trans. Consum. Electron.*, vol. 64, no. 3, pp. 339–347, Aug. 2018.

[5] W. Han, K. T. Chau, C. Jiang, and W. Liu, "All-metal domestic induction heating using single-frequency double-layer coils," *IEEE Trans. Magn.*, vol. 54, no. 11, pp. 1–5, Nov. 2018.

[6] J. Serrano, J. Acero, I. Lope, C. Carretero, and J. M. Burdio, "A flexible cooking zone composed of partially overlapped inductors," *IEEE Trans. Ind. Electron.*, vol. 65, no. 10, pp. 7762–7771, Oct. 2018.

[7] O. Lucia, D. Navarro, P. Guillen, H. Sarnago, and S. Lucia, "Deep learning-based magnetic coupling detection for advanced induction heating appliances," *IEEE Access*, vol. 7, no. 12, pp. 181668–181677, Dec. 2019.

[8] J. Villa, L. A. Barrágan, J. I. Artigas, D. Navarro, A. Domínguez, and T. Cabeza, "SoC-based in-cycle load identification of induction heating appliances," *IEEE Trans. Ind. Electron.*, vol. 68, no. 8, pp. 6762–6772, Aug. 2021.

[9] A. Bono-Nuez, B. Martin-del-Brio, C. Bernal-Ruiz, F. J. Perez-Cebolla, A. Martinez-Iturbe, and I. Sanz-Gorrachategui, "The inductor as a smart sensor for material identification in domestic induction cooking," *IEEE Sensors J.*, vol. 18, no. 6, pp. 2462–2470, Mar. 2018.

[10] J. Villa, J. I. Artigas, J. R. Beltrán, A. D. Vicente, and L. A. Barragán, "Analysis of the acoustic noise spectrum of domestic induction heating systems controlled by phase-accumulator modulators," *IEEE Trans. Ind. Electron.*, vol. 66, no. 8, pp. 5929–5938, Aug. 2019.

[11] J. Acero, I. Lope, C. Carretero, and J. M. Burdio, "Analysis and modeling of the forces exerted on the cookware in induction heating applications," *IEEE Access*, vol. 8, no. 7, pp. 131178–131187, Jul. 2020.

[12] I. Lope, J. Acero, J. M. Burdío, C. Carretero, and R. Alonso, "Design and implementation of PCB inductors with litz-wire structure for conventional-size large-signal domestic induction heating applications," *IEEE Trans. Ind. Appl.*, vol. 51, no. 3, pp. 2434–2442, Jul. 2015.

[13] C. Carretero, I. Lope, and J. Acero, "Magnetizable concrete flux concentrators for wireless inductive power transfer applications," *IEEE J. Emerg. Sel. Topics Power Electron.*, vol. 8, no. 3, pp. 2696–2706, Sep. 2020.

[14] F. Sanz, C. Sagues, and S. Llorente, "Induction heating appliance with a mobile double-coil inductor," *IEEE Trans. Ind. Appl.*, vol. 51, no. 3, pp. 1945–1952, May 2015.

[15] J. Acero, I. Lope, C. Carretero, and J. M. Burdio, "Adapting of non-metallic cookware for induction heating technology via thin-layer non-magnetic conductive coatings," *IEEE Access*, vol. 8, no. 1, pp. 11219–11227, Jan. 2020.

[16] *The Qi specification: Power Class 0 Specification. Version 1.2.3*, Standard Rev. Version 1.2.3, Wireless Power Consortium, 2017. [Online]. Available: https://www.wirelesspowerconsortium.com/

[17] M. Kim, H.-P. Park, and J.-H. Jung, "Practical design methodology of IH and IPT dual-functional apparatus," *IEEE Trans. Power Electron.*, vol. 35, no. 9, pp. 8897–8901, Sep. 2020.

[18] E. Plumed, J. Acero, I. Lope, and J. M. Burdío, "Design methodology of high performance domestic induction heating systems under worktop," *IET Power Electron.*, vol. 13, no. 2, pp. 300–306, Feb. 2020.

[19] J. S. Choi, S. Y. Jeong, B. G. Choi, S.-T. Ryu, C. T. Rim, and Y.-S. Kim, "Air-gap-insensitive IPT pad with ferromagnetic and conductive plates," *IEEE Trans. Power Electron.*, vol. 35, no. 8, pp. 7863–7872, Aug. 2020.

[20] W. Zhong, C. K. Lee, and S. Y. R. Hui, "General analysis on the use of Tesla's resonators in domino forms for wireless power transfer," *IEEE Trans. Ind. Electron.*, vol. 60, no. 1, pp. 261–270, Jan. 2013.

[21] W. X. Zhong, C. Zhang, X. Liu, and S. Y. R. Hui, "A methodology for making a three-coil wireless power transfer system more energy efficient than a two-coil counterpart for extended transfer distance," *IEEE Trans. Power Electron.*, vol. 30, no. 2, pp. 933–942, Feb. 2015.

[22] J. Zhang, X. Yuan, C. Wang, and Y. He, "Comparative analysis of two-coil and three-coil structures for wireless power transfer," *IEEE Trans. Power Electron.*, vol. 32, no. 1, pp. 341–352, Jan. 2017.

[23] Y. Li, J. Hu, M. Liu, Y. Chen, K. W. Chan, Z. He, and R. Mai, "Reconfigurable intermediate resonant circuit based WPT system with load-independent constant output current and voltage for charging battery," *IEEE Trans. Power Electron.*, vol. 34, no. 3, pp. 1988–1992, Mar. 2019.

[24] Z.-J. Liao, Y. Sun, Z.-H. Ye, C.-S. Tang, and P.-Y. Wang, "Resonant analysis of magnetic coupling wireless power transfer systems," *IEEE Trans. Power Electron.*, vol. 34, no. 6, pp. 5513–5523, Jun. 2019.

[25] W. Han, K. T. Chau, and Z. Zhang, "Flexible induction heating using magnetic resonant coupling," *IEEE Trans. Ind. Electron.*, vol. 64, no. 3, pp. 1982–1992, Mar. 2017.

[26] W. Han, K. T. Chau, Z. Zhang, and C. Jiang, "Single-source multiple-coil homogeneous induction heating," *IEEE Trans. Magn.*, vol. 53, no. 11, pp. 1–6, Nov. 2017.

[27] E. Plumed, I. Lope, and J. Acero, "Induction heating adaptation of a different-sized load with matching secondary inductor to achieve uniform heating and enhance vertical displacement," *IEEE Trans. Power Electron.*, vol. 36, no. 6, pp. 6929–6942, Jun. 2021.

[28] C. Viellard, A. Romann, U. Lott, and N. Kuster, "B-field exposure from induction cooking appliances," in *Proc. 28th Annu. Meeting Bioelectromagnetics Soc.*, Cancun, Mexico, Jun. 2006, pp. 139–140.

[29] *ICNIRP Guidelines for Limiting Exposure to Time-Varying Electric, Magnetic and Electromagnetic Fields (Up to 300 GHz)*, Standard, International Commission on Non-Ionizing Radiation Protection, 1998. [Online]. Available: https://www.icnirp.org/cms/upload/publications/ICNIRPemfgdl.pdf

[30] *IEC 62233 Measurement Methods for Electromagnetic Fields of Household Appliances and Similar Apparatus With Regard to Human Exposure*, Standard IEC 62233:2005, International Electrotechnical Commission (EIC), 2005. [Online]. Available: https://webstore.iec.ch/publication/6618

[31] *UNE-EN 62233 Métodos de Medida de Los Campos Electromagnéticos de Los Aparatos Electrodomésticos y Análogos en Relación con la Exposición Humana*, Standard UNE-EN 62233:2009, Asociación Española de Normalización y Certificación (AENOR), 2009. [Online]. Available: https://www.en.aenor.com/

[32] C. Carretero, R. Alonso, and J. Acero, "Interference emission estimation of domestic induction cookers based on finite-element simulation," *IEEE Trans. Electromagn. Compat.*, vol. 58, no. 4, pp. 993–999, Aug. 2016.

[33] L. A. Barragan, D. Navarro, J. Acero, I. Urriza, and J. M. Burdio, "FPGA implementation of a switching frequency modulation circuit for EMI reduction in resonant inverters for induction heating appliances," *IEEE Trans. Ind. Electron.*, vol. 55, no. 1, pp. 11–20, Jan. 2008.

[34] F. Pareschi, R. Rovatti, and G. Setti, "EMI reduction via spread spectrum in DC/DC converters: State of the art, optimization, and tradeoffs," *IEEE Access*, vol. 3, pp. 2857–2874, 2015.

[35] H. Rickli, M. Facchini, H. Brunner, P. Ammann, M. Sagmeister, G. Klaus, W. Angehrn, R. Luechinger, and F. Duru, "Induction ovens and electromagnetic interference: What is the risk for patients with implanted pacemakers?" *Pacing Clin. Electrophysiol.*, vol. 26, no. 7, pp. 1494–1497, Jul. 2003.

[36] J. Miyakoshi, E. Horiuchi, T. Nakahara, and T. Sakurai, "Magnetic fields generated by an induction heating (IH) cook top do not cause genotoxicity *in vitro*," *Bioelectromagnetics*, vol. 28, no. 7, pp. 529–537, Oct. 2007.

[37] B. Kos, B. Valič, D. Miklavčič, T. Kotnik, and P. Gajšek, "Pre- and post-natal exposure of children to EMF generated by domestic induction cookers," *Phys. Med. Biol.*, vol. 56, no. 19, pp. 6149–6160, Oct. 2011.

[38] International Commission on Non-Ionizing Radiation Protection (ICNIRP), "Guidelines for limiting exposure to time-varying electric and magnetic fields (1 Hz to 100 kHz)," *Health Phys.*, vol. 99, no. 6, p. 10, 2010. [Online]. Available: https://journals.lww.com/health-physics/Fulltext/2010/12000/GUIDELINES_FOR_LIMITING_EXPOSURE_TO_TIME_VARYING.26.aspx

[39] C. Carretero, J. Acero, R. Alonso, and J. M. Burdío, "Normal-mode decomposition of surface power distribution in multiple-coil induction heating systems," *IEEE Trans. Magn.*, vol. 52, no. 2, pp. 1–8, Feb. 2016.

[40] C. Carretero, J. Acero, and R. Alonso, "TM-TE decomposition of power losses in multi-stranded litz-wires used in electronic devices," *Prog. Electromagn. Res.*, vol. 123, pp. 83–103, Jan. 2012.

EMILIO PLUMED (Member, IEEE) received the M.Sc. degree in industrial engineering from the Universidad de Zaragoza, Zaragoza, Spain, in 2016, where he is currently pursuing the Ph.D. degree in electronic engineering with the Department of Electronic Engineering and Communications. His research interests include electromagnetic modeling of induction heating (IH) systems and hybrid IH and wireless power transfer systems.

IGNACIO LOPE (Member, IEEE) received the M.Sc. degree in electrical engineering and the Ph.D. degree in power electronics from the Universidad de Zaragoza, Zaragoza, Spain, in 2010 and 2015, respectively. He is currently with BSH Home Appliances, Zaragoza, where he is involved in several projects focusing on developing domestic induction heating appliances. He is also an Adjunct Professor with the Department of Applied Physics, Universidad de Zaragoza. His current research interests include electromagnetic modeling of inductive coupled contactless energy transfer systems and loss modeling of magnetic devices.

JESUS ACERO (Senior Member, IEEE) received the M.Sc. and Ph.D. degrees in electrical engineering from the Universidad de Zaragoza, Zaragoza, Spain, in 1992 and 2005, respectively. From 1992 to 2000, he worked in several industry projects, especially focused on custom power supplies for research laboratories. Since 2000, he has been with the Department of Electronic Engineering and Communications, Universidad de Zaragoza, where he is currently a Professor. His main research interests include resonant converters for induction heating applications, inductive-type load modeling, and electromagnetic modeling. He is a member of the IEEE Power Electronics, Industrial Electronics and Magnetics Societies. He is also a member of the Instituto de Investigación en Ingeniería de Aragon (I3A).